Adaptive Vision-Based Leader–Follower Formation Control of Mobile Robots

Hesheng Wang, *Senior Member, IEEE*, Dejun Guo, *Student Member, IEEE*, Xinwu Liang, Weidong Chen, Guoqiang Hu, and Kam K. Leang, *Member, IEEE*

***Abstract*—This paper focuses on the problem of vision-based leader–follower formation control of mobile robots. The proposed adaptive controller only requires the image information from an uncalibrated perspective camera mounted at any position and orientation (attitude) on the follower robot. Furthermore, the approach does not depend on the relative position measurement and communication between the leader and follower. First, a new real-time observer is developed to estimate the unknown intrinsic and extrinsic camera parameters as well as the unknown coefficients of the plane where the feature point moves relative to the camera frame. Second, the Lyapunov method is employed to prove the stability of the closed-loop system, where it is shown that convergence of the image error is guaranteed. Finally, the performance of the approach is demonstrated through physical experiments and experimental results.**

***Index Terms*—Adaptive control, mobile robot, tracking control, visual servo.**

I. Introduction

SINCE the 1990s, mobile robot formation control has been an active area of research. Robots are needed to maintain a desired formation in applications such as surveillance, reconnaissance, search and rescue, and transportation. One approach to the formation control problem is to divide the robots into groups of two-robot systems, each consisting of one leader and one follower. Then, one robot is considered as the overall formation "leader," and the rest of the robots are labeled as the "followers." All followers maintain the desired relative positions with respect to each of their leaders defined by the two-robot system. Such a configuration is relatively reliable when the graph describing the sensing topology combines the two-robot systems.

Many studies focus on the target-tracking problem [1]–[14], where the advantages of on-board cameras are exploited in many works. In particular, low-cost on-board cameras are highly desired and employed widely for vision-based motion control of mobile robots [1]–[12]. In many cases, robots usually match and track special features [1]–[7] or recognize a particular color on the target [8], [9] for motion control. In fact, the geometric information relative to the target is measured based on the detected image information. Then, motion control is achieved using approaches such as proportional-integral derivative [1], the feedback linearization [5], [8], [11], and adaptive control [2], [12], [13].

Vision-based leader–follower approaches can be classified into two categories: 1) position-based visual servo (PBVS) and (2) image-based visual servo (IBVS). In PBVS [1]–[9], an on-board camera is used to extract the relative distance and bearing between the leader and follower. For example, using this approach, Poonawala *et al.* [3] developed a novel controller independent of measurement and estimation of the leader's velocity. In their paper, the centers of four special blobs on the leader were identified from the segmented binary image captured by a perspective camera. The accurate relative geometric information was calculated based on both the known size of the mark and the carefully calibrated camera parameters. Dani *et al.* [4] obtained the relative pose and velocity of the leader using a geometric pose estimation technique and a nonlinear velocity estimation strategy. They based their work on the condition that the perspective camera should be calibrated and that the distance between the leader and follower is measurable. Chueh *et al.* [7] identified a distinctive logo on the leader from a perspective image and measured the 2-D coordinates of one single point on the leader relative to the follower frame. Das *et al.* [8] exploited a calibrated omnidirectional camera, and then, used an extended Kalman filter (EKF) to estimate the velocity of the leader. Fidan *et al.* [9] proposed a method to detect the upper border and the bottom border of a colored cylinder on the leader. The distances were measured based on the known height of the cylinder and

Manuscript received March 29, 2016; revised July 13, 2016 and August 26, 2016; accepted September 24, 2016. Date of publication November 22, 2016; date of current version March 8, 2017. This work was supported in part by the National Natural Science Foundation of China under Grant U1613218, Grant 61473191, Grant 61503245, Grant 61221003, and Grant 61673272, in part by the Science and Technology Commission of Shanghai Municipality under Grant 15111104802, in part by the Shanghai Sailing Program under Grant 15YF1406300, and in part by the State Key Laboratory of Robotics and System, Harbin Institute of Technology.

H. Wang is with the Department of Automation, Shanghai Jiao Tong University, and the Key Laboratory of System Control and Information Processing, Ministry of Education of China, Shanghai 200240, China, and also with the State Key Laboratory of Robotics and System, Harbin Institute of Technology, Harbin 150001, China (email: wanghesheng@sjtu.edu.cn).

D. Guo and K. K. Leang are with the DARC (Design, Automation, Robotics & Control) Lab, University of Utah Robotics Center, Salt Lake City, UT 84112 USA (e-mail: dejunguo422@gmail.com; kam.k.leang@utah.edu).

X. Liang is with the School of Aeronautics and Astronautics, Shanghai Jiao Tong University, Shanghai 200240, China (e-mail: xinwu113@163.com).

W. Chen is with the Department of Automation, Shanghai Jiao Tong University, and the Key Laboratory of System Control and Information Processing, Ministry of Education of China, Shanghai 200240, China (e-mail: wdchen@sjtu.edu.cn)

G. Hu is with the School of Electrical and Electronic Engineering, Nanyang Technological University (NTU), Singapore 639798 (e-mail: gqhu@ntu.edu.sg).

Color versions of one or more of the figures in this paper are available online at http://ieeexplore.ieee.org.

Digital Object Identifier 10.1109/TIE.2016.2631514

the known intrinsic parameters of a perspective camera. It is noted that some of the drawbacks of PBVS methods include the measurement/reconstruction of the distance and bearing or pose is computationally demanding and the technique suffers from low accuracy due to calibration error.

To overcome the drawbacks of PBVS leader–follower approaches, IBVS was developed. In this case, the control variables (outputs) are the 2-D coordinates of a point on the image plane (in pixels). For example, Vidal *et al.* [5] designed an IBVS controller using a calibrated on-board omnidirectional camera. The optical flow method was used to identify the leader. In their paper, the follower had to identify a static point fixed to the world frame at all times in order to compensate for the unknown velocity of the leader. In general, the IBVS technique has three obvious advantages. First, rather than measuring the relative distance, pose, and velocity of the leader for motion control, the objective is to control the follower robot to keep the leader's position fixed at a desired position in the image frame, making the approach more efficient. Second, errors due to sensor modeling and camera calibration can be avoided [15]. Third, the point in the image can essentially travel in a straight line toward the desired position without leaving the field of view of the camera [15].

Despite the advances made and the advantages of vision-based control methods, they all still suffer from the drawbacks related to camera calibration [1]–[12]. In the multirobot case, in particular, the dependence on camera calibration is significant. In addition, designs that require communication devices for estimating velocity of the leader increases the overall system cost, requires space on the follower to support the hardware, and limits operating performance due to packet loss and poor communication. Therefore, it is necessary to develop a vision-based leader–follower approach for mobile robots under the IBVS framework that does not require camera calibration and communication between the leader and the follower.

In the recent years, researchers have focused their attention on improving the design of vision-based control systems. For instance, Garcia de Marina *et al.* [16] achieved formation control of unicycles with uncalibrated sensors. Mariottini *et al.* [10] and Morbidi *et al.* [11] proposed a PBVS approach that relaxed the need to calibrate an omnidirectional camera. Instead, the relative distance was estimated by an EKF and immersion-and-invariance-based observer. The relative bearing was calculated by mutual measurements through two uncalibrated omnidirectional cameras mounted vertically at the rotation centers of the follower and leader. However, the leader's velocity was determined from the communication between the leader and follower. In other cases, the control algorithms [6], [17] cannot avoid the need for camera calibration and the target's velocity. Wang *et al.* [17] showed that an eye-in-hand holonomic manipulator can track a moving object with unknown motion, but the camera had to be calibrated. Recently, an uncalibrated high-flying camera was applied to monitor, track, and control a low-flying unmanned aerial vehicle or mobile robot [18]. The researchers developed an adaptive-repetitive control system for the uncalibrated camera system to track periodic reference trajectories in the image frame. In general, there has been limited success with the realization of a vision-based leader–follower control algorithm that does not rely on camera calibration and leader–follower communication.

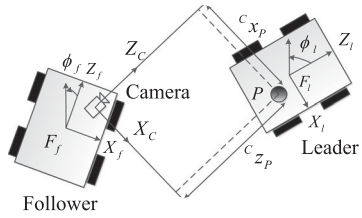

Fig. 1. Vision-based leader–follower system with relevant coordinates and variables and *P* denotes the point on the leader.

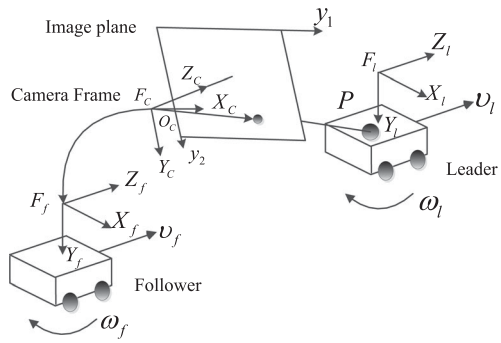

Fig. 2. Projection model of a pin-hole camera.

To reduce the complexities associated with extrinsic camera parameters and avoid camera calibration, many vision-based leader–follower approaches require the camera to be locate at the center of rotation of the mobile robot [8], [11]. By doing this, however, it limits where the camera can be place on the robot. Moreover, this arrangement also limits the location of the feature point on the leader robot, and difficulties arise when the special feature point at the center of rotation is not detectable.

The main contributions of the research described in this paper are fourfold. First is the design of an online adaptive observer, which can estimate the unknown intrinsic and extrinsic parameters of the camera as well as the unknown coefficients of the plane in which the feature point moves relative to the camera frame. In fact, the camera can be mounted at any position and orientation on the robot. Second is the design and implementation of a new adaptive image-based controller that is independent of the leader's velocity. Third is the analysis of the stability of the closed-loop system using the Lyapunov approach. It is shown that the convergence of the image errors and the formation error are guaranteed. Finally, the fourth is the performance of the approach is demonstrated through physical experiments and experimental results.

II. Problem Formulation and Kinematics Modeling

A. Notation and Reference Frames

The following notation is used in this paper. A bold letter represents a matrix or a vector. Otherwise, standard face letters represent a scalar quantity. The follower, leader, camera, and feature point are denoted by the letters *f*, *l*, *C,* and *P,* respectively. The presuperscript represents the frame that the variable is relative to, e.g.,. ${}^{f}x_P$ denotes the coordinate of feature point *P* along X_f axis).

The coordinate frames are illustrated in Figs. 1 and 2. The world frame is fixed on the ground. The origins of the follower

frame F_f and the leader frame F_l are located at the center of rotation of the follower F_f and the leader, respectively. The axis Z_l and Z_f are aligned with the forward direction of the robots. The planes $Z_lO_lX_l$ and $Z_fO_fX_f$ are parallel to the ground plane. The robot's linear velocity is defined along its Z-axis, and its angular velocity is orthogonal to the ground plane. The on-board camera is assumed to be a pin-hole camera with a perspective projection.

B. Problem Statement

Given a desired position $\mathbf{y}_d$ defined on the image plane of the follower robot and let the feature point P on the leader robot be in the field of view of the follower's camera. The objective is to design a kinematic controller to position the follower robot such that the feature point P is guaranteed to converge asymptotically to an arbitrarily small circle around the desired position under the following conditions: 1) an uncalibrated camera is mounted on the follower with an arbitrary position and orientation; 2) the feature point P can be arbitrarily located on the leader (with unknown position and height); and 3) there is no communication between leader and follower.

Assumption 1: For practical purposes, the velocity and acceleration of the leader are bounded, i.e.,

$$|v_l| \leq \bar{v}_l, |\dot{v}_l| \leq \bar{\dot{v}}_l, |\omega_l| \leq \bar{\omega}_l, |\dot{\omega}_l| \leq \bar{\dot{\omega}}_l$$

where v_l and ω_l are linear and angular velocity of the leader, respectively, $\dot{v}_l$ and $\dot{\omega}_l$ are linear and angular acceleration of the leader, respectively, and $\bar{v}_l$, $\bar{\omega}_l$, $\bar{\dot{v}}_l$, and $\bar{\dot{\omega}}_l$ are their upper bounds, respectively.

Assumption 2: The projection of the feature point P is always in the field of view of the follower's camera. The follower and the leader move on the ground plane. The plane where the feature point P moves does not pass through the optical center of the camera.

Remark 1: The formation error is defined as the 2-D position error of P with respective to F_f [7], rather than F_l. The reason for this is that this approach guarantees lower control effort and much smoother trajectories for the follower than the one defined in frame F_l [19]. Additionally, this definition is better suited and more practical for the IBVS approach presented in this paper.

Remark 2: The desired image point can be obtained in a simple way: By recording it with an on-board camera when the leader locates itself at a desired position with respect to F_f. This situation is known as the "teach-by-showing" approach.

Remark 3: Several two-robot systems, within a group of multiple robots, can form various formations. A desired formation can be described by a tree structure, and thus, all robots are treated as nodes. The group leader is the root node and moves independent of the others. Each robot has only one one-way edge connected to the other robot. Then, as long as every robot follows its leader, with a desired pose, the desired formation can be achieved.

C. Kinematics

In the following, the 3-D coordinates of feature point P relative to F_f is denoted by ${}^f\mathbf{P}_P$. Let γ denote the relative orientation and $\mathbf{n}$ denote the 3-D coordinates of the feature point P relative to F_l. It is noted that the mobile robots here are velocity-controlled nonholonomic systems and they have two independent inputs, the linear velocity v_i along axis Z_i and the angular velocity ω_i along axis Y_i $(i = l, f)$. Let $\mathbf{u}_i = [\,v_i \quad \omega_i\,]^T$. Therefore, the time derivative of ${}^f\mathbf{P}_P$ is given by

$${}^f\dot{\mathbf{P}}_P = \mathbf{J}_{\mathrm{ff}}\left({}^f\mathbf{P}_P\right)\mathbf{u}_f + \mathbf{J}_{\mathrm{lf}}\left(\mathbf{n}, \gamma\right)\mathbf{u}_l, \dot{\gamma} = \omega_l - \omega_f \tag{1}$$

where the Jacobian matrices $\mathbf{J}_{\mathrm{ff}}$ and $\mathbf{J}_{\mathrm{lf}}$ are shown in the first item in the Appendix.

Fig. 2 shows the perspective projection model of a pin-hole camera mounted on the follower. Let ${}^C\mathbf{P}_P$ denote the 3-D coordinates of P with respect to frame F_C. Then, the homogeneous transformation of F_C with respect to F_f is denoted by ${}^f\mathbf{g}_C$, and this represents the extrinsic parameters of the camera, hence

$$\begin{bmatrix} {}^C\mathbf{P}_P \\ 1 \end{bmatrix} = \left({}^f\mathbf{g}_C\right)^{-1}\begin{bmatrix} {}^f\mathbf{P}_P \\ 1 \end{bmatrix}. \tag{2}$$

Taking the time derivate of (2) and substituting for ${}^f\dot{\mathbf{P}}_P$ from the aforementioned results in

$${}^C\dot{\mathbf{P}}_P = \mathbf{J}_{\mathrm{fC}}\left({}^C\mathbf{P}_P\right)\mathbf{u}_f + \mathbf{J}_{\mathrm{lC}}\left(\gamma\right)\mathbf{u}_l \tag{3}$$

where the Jacobian matrices $\mathbf{J}_{\mathrm{fC}}$ and $\mathbf{J}_{\mathrm{lC}}$ are shown in the first item in Appendix.

Next, the projection of P on the image plane is denoted by a 2×1 vector $\mathbf{y}(t) = [\,y_1 \;\; y_2\,]^T$. The projection equation describing the mapping relation between $\mathbf{y}$ and ${}^C\mathbf{P}_P$ is given by

$$\begin{bmatrix} \mathbf{y} \\ 1 \end{bmatrix} = \frac{1}{{}^C z_P}\mathbf{A}\,{}^C\mathbf{P}_P. \tag{4}$$

By convention, it is assumed that the intrinsic matrix A is

$$\mathbf{A} = \begin{bmatrix} \lambda_1 & 0 & y_{1o} \\ 0 & \lambda_2 & y_{2o} \\ 0 & 0 & 1 \end{bmatrix}. \tag{5}$$

Here, $[\,y_{1o} \quad y_{2o}\,]^T$ consists of the coordinates of the principle point on the image plane. λ_1 and λ_2 are the product of the focal length and the magnifications in the y_1 and y_2 directions, respectively. Moreover, ${}^C z_P$ in (4) represents the depth of the feature point P with respect to frame F_C. Combining (3) and (4) results in

$$\dot{\mathbf{y}} = \mathbf{J}_{\mathrm{fy}}\left({}^C z_P^{-1}, \mathbf{y}\right)\mathbf{u}_f + \mathbf{J}_{\mathrm{ly}}\left({}^C z_P^{-1}, \gamma\right)\mathbf{u}_l, \dot{\gamma} = \omega_l - \omega_f. \tag{6}$$

Next, the unknown depth ${}^C z_P$ is removed from the kinematics. According to Assumption 2, both robots move on the ground plane. Thus, the feature point P moves on a fixed plane with respect to frame F_C. Therefore, the plane equation can be exploited to express this constraint, i.e., $a\,{}^C x_P + b\,{}^C y_P + c\,{}^C z_P = 1$, where a, b, and c are the coefficients of the plane equation. Then, after eliminating ${}^C x_P$ and ${}^C y_P$ with the help of (4), the depth information of the feature point P with respect to F_C can be expressed as

$$\frac{1}{{}^C z_P} = \frac{a}{\lambda_1}(y_1 - y_{1o}) + \frac{b}{\lambda_2}(y_2 - y_{2o}) + c. \tag{7}$$

Replacing $1/{}^C z_P$ in (6) with (7), the kinematics of the system without ${}^C z_P$ is obtained, hence,

$$\dot{\mathbf{y}} = \mathbf{H}(\mathbf{y})\mathbf{u}_f + \underbrace{\mathbf{G}(\gamma)\mathbf{u}_l}_{\mathbf{F}(\gamma, v_l, \omega_l)}, \dot{\gamma} = \omega_l - \omega_f. \tag{8}$$

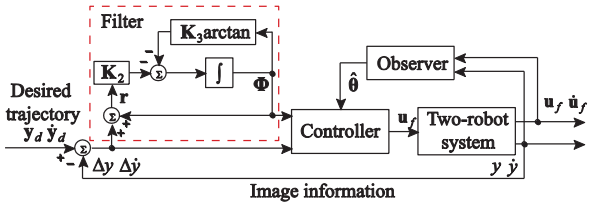

Fig. 3. Control block diagram.

Remark 3: The constant parameters in $\mathbf{H}(\mathbf{y}) \in \Re^{2\times 2}$ can be linearized. First, the unknown constant parameters are denoted by $\theta \in \Re^{16\times 1}$. This includes the camera parameters (*i.e.,* the elements in $\mathbf{A}$ and ${}^{f}\mathbf{g}_{C}$) and the coefficients of plane equation a, b, and c. Then, $\mathbf{H}(\mathbf{y})$ can be revised as follows:

$$\mathbf{H}(\mathbf{q},\mathbf{y}) = \begin{bmatrix} \theta_1 y_1 + \theta_2 y_2 + \theta_3 y_1 y_2 + \theta_4 y_1^2 + \theta_5 \\ \theta_6 y_1 + \theta_7 y_2 + \theta_8 y_1 y_2 + \theta_9 y_1^2 + \theta_{10} \\ \theta_{11} y_1 + \theta_{12} y_2 + \theta_4 y_1 y_2 + \theta_3 y_2^2 + \theta_{13} \\ \theta_{14} y_1 + \theta_{15} y_2 + \theta_9 y_1 y_2 + \theta_8 y_2^2 + \theta_{16} \end{bmatrix}$$

where θ_i denote the *ith* row of θ.

Remark 4: $\mathbf{F}(\mathbf{y},\gamma,\upsilon_l,\omega_l) \in \Re^{2\times 1}$ is a vector, which contains the time-variant elements, such as $\mathbf{y}$, γ, and $\mathbf{u}_l$, parts of the unknown parameters θ and $\mathbf{n}$. For this problem, it is difficult to measure γ and $\mathbf{u}_l$. Therefore, it is challenging to cope with the second term $\mathbf{F}$ at the right-hand side of (8), when the controller is designed as described in Section III-B.

Property 1: For any 2-D vector $\mathbf{u} = [\upsilon \quad \omega]^T$, $\mathbf{H}(\theta,\mathbf{y})\mathbf{u}$ and $\dot{\mathbf{H}}(\theta,\mathbf{y},\dot{\mathbf{y}})\mathbf{u}$ can be parameterized in the following linear form:

$$\mathbf{H}(\theta,\mathbf{y})\mathbf{u} = \mathbf{M}(\mathbf{y},\mathbf{u})\theta, \qquad \dot{\mathbf{H}}(\theta,\mathbf{y},\dot{\mathbf{y}})\mathbf{u} = \mathbf{N}(\mathbf{y},\dot{\mathbf{y}},\mathbf{u})\theta \tag{9}$$

where $\mathbf{M}(\mathbf{y},\mathbf{u})$ and $\mathbf{N}(\mathbf{y},\dot{\mathbf{y}},\mathbf{u}) \in \Re^{2\times 16}$ are the regressor matrices without containing any constant unknown parameters $\theta \in \Re^{16\times 1}$.

III. Adaptive Vision-Based Formation Control

A. Controller Design

The control block diagram is shown in Fig. 3. The expected image-based controller should generate the follower's linear and angular velocity without the need for the velocity of the leader. To design this controller, the image-based error containing the image position error and the image velocity error are exploited as the feedback signal. In addition, a filter is designed to generate an image-based signal to compensate for the absence of the unknown matrix $\mathbf{F}$ mentioned in Remark 4.

First, the image-based error $\mathbf{r}$ is defined as

$$\mathbf{r} = \mathbf{s}\Delta\dot{\mathbf{y}} + \mathbf{k}\Delta\mathbf{y} + \mathbf{\Phi} \tag{10}$$

where the image error is $\Delta\mathbf{y} = [y_1 - y_{1d} \quad y_2 - y_{2d}]^T$. Since the desired position of P with respect to F_f is constant, the desired position of the feature point on the image plane $\mathbf{y}_d$ is constant. Then, the desired velocity $\dot{\mathbf{y}}_d$ is zero and $\Delta\dot{\mathbf{y}} = [\dot{y}_1 \quad \dot{y}_2]^T$ represents the image velocity error. The signal generated by an image-based filter, which is inspired by filters applied in [22] and [23] is given by $\mathbf{\Phi} = [\Phi_1 \ \Phi_2]^T$. Next, the image-based filter is designed as

$$\dot{\mathbf{\Phi}} = -\mathbf{K}_3\mathbf{\Psi} - \mathbf{K}_2\mathbf{r}, \qquad \mathbf{\Phi}(0) = \mathbf{0}_{2\times 1} \tag{11}$$

where $\mathbf{\Psi} = [\arctan\Phi_1 \ \arctan\Phi_2]^T$, and $\mathbf{s}$, $\mathbf{k}$, $\mathbf{K}_2$, and $\mathbf{K}_3 \in \Re^{2\times 2}$ are positive-definite and diagonal gain matrices. The differential of the image-based error $\mathbf{r}$ is $\dot{\mathbf{r}} = \mathbf{s}\Delta\ddot{\mathbf{y}} + \mathbf{k}\Delta\dot{\mathbf{y}} + \dot{\mathbf{\Phi}}$. Substituting (8) into it, $\dot{\mathbf{r}}$ becomes

$$\dot{\mathbf{r}} = \mathbf{s}\mathbf{H}\dot{\mathbf{u}}_f + (\mathbf{s}\dot{\mathbf{H}} + \mathbf{k}\mathbf{H})\mathbf{u}_f + \mathbf{s}\dot{\mathbf{F}} + \mathbf{k}\mathbf{F} - \mathbf{K}_3\mathbf{\Psi} - \mathbf{K}_2\mathbf{r} \tag{12}$$

which can be considered as the vision-based leader–follower system expressed in the new coordinate and the inputs are given by $\dot{\mathbf{u}}_f$.

The following controller is proposed:

$$\dot{\mathbf{u}}_f = (\mathbf{s}\hat{\mathbf{H}})^{-1}\Big(-\mathbf{K}_1\mathbf{r} + \mathbf{\Gamma}_1^{-1}\mathbf{K}_2\mathbf{\Pi} + \mathbf{K}_3\mathbf{\Psi} - \left(\mathbf{s}\hat{\dot{\mathbf{H}}} + \mathbf{k}\hat{\mathbf{H}}\right)\mathbf{u}_f - \mathbf{K}_4\left\|\frac{\partial U}{\partial\hat{\theta}}t\right\|\mathbf{r}\Big) \tag{13}$$

where $\mathbf{s}\hat{\mathbf{H}}(\hat{\theta},\mathbf{y})$ and $\hat{\dot{\mathbf{H}}}(\hat{\theta},\mathbf{y},\dot{\mathbf{y}})$ are calculated using the estimated parameters $\hat{\theta} \in \Re^{16\times 1}$, $\mathbf{\Pi} = [\tanh(\alpha_1\Phi_1) \ \tanh(\alpha_2\Phi_2)]^T$, α_1 and α_2 are positive gains, and $\mathbf{\Gamma}_1, \mathbf{K}_1, \mathbf{K}_4 \in \Re^{2\times 2}$ are positive-definite and diagonal gain matrices. $\mathbf{K}_4||\partial U/\partial\hat{\theta}||\mathbf{r}$ serves as a potential force [23] that can push the estimated parameters away from the singularity of the matrix $\mathbf{s}\hat{\mathbf{H}}(\hat{\theta},\mathbf{y})$ and it guarantees the existence of the inverse of $\mathbf{s}\hat{\mathbf{H}}(\hat{\theta},\mathbf{y})$. However, this only works when the determinant $p(t) = |\mathbf{s}\hat{\mathbf{H}}(\hat{\theta},\mathbf{y})|$ approaches to zero; otherwise, $\mathbf{K}_4||\partial U/\partial\hat{\theta}||\mathbf{r}$ is zero. For the details of the definition of the repulsive potential field $U(\hat{\theta})$ and the potential force $\partial U/\partial\hat{\theta}$, please find this in the third item in Appendix.

The controller given by (13) shows an update law for the follower's velocity, and $\mathbf{u}_f$ can be calculated by numerical integration. In fact, a low-level servo system creates the control signals to drive the wheels of the robot to achieve the desired linear and angular velocities.

B. Observer Design

The observer is designed to estimate the unknown parameters q in the controller given by (13) online. The controller is designed based on the adaptive control theory [22], where the estimated parameters can be linearly parameterized in the kinematic system (12) (Property 1), hence

$$\dot{\hat{\theta}} = \mathbf{\Gamma}_2^{-1}\left[\left(\mathbf{M}^T(\mathbf{y},\dot{\mathbf{u}}_f)\mathbf{s} + \mathbf{N}^T(\mathbf{y},\dot{\mathbf{y}},\mathbf{u}_f)\mathbf{s} + \mathbf{M}^T(\mathbf{y},\mathbf{u}_f)\mathbf{k}\right)\mathbf{\Gamma}_1\mathbf{r} + \mathbf{r}^T\mathbf{r}\mathbf{K}_5\partial U/\partial\hat{\theta}\right] \tag{14}$$

where the first three terms in (14) come from the Slotine-Li [22] algorithm and Property 1, $\mathbf{\Gamma}_2, \mathbf{K}_5 \in \Re^{16\times 16}$ are positive-definite and diagonal gain matrices, and $\partial U/\partial\hat{\theta} \in \Re^{16\times 1}$ is the potential force (mentioned in Appendix), which pushes the estimation parameters away from the singularity of $\mathbf{s}\hat{\mathbf{H}}(\hat{\theta},\mathbf{y})$. The observer depends on the current image position and velocity of the feature point, as well as the velocity and acceleration of the follower.

The nonlinear observer (14) provides an update law of the estimated parameters, and $\hat{\theta}$ can be calculated by numerical integration.

C. Stability Analysis

Theorem 1: Assume that the system described by (12) satisfies Assumptions 1 and 2, $\gamma(t_0) \neq \pm\pi$ and ${}^{\upsilon_l}f z_{\mathrm{Pd}} > 0$. The norm of the initial values of $\mathbf{r}$, F, and $\tilde{q}$ have upper limits. With the controller proposed in (13) and the observer presented in (14), the closed-loop system is stable. The convergences of the image errors $\Delta\mathbf{y}$, $\Delta\dot{\mathbf{y}}$, and the filtered error F are guaranteed. The internal dynamics of the system are stable, *i.e.*, the relative orientation γ is bounded.

Proof: Introduce the following positive function:

$$V = \frac{1}{2}\mathbf{r}^T\boldsymbol{\Gamma}_1\mathbf{r} + \mathbf{L}^T\boldsymbol{\Lambda}\mathbf{L} + \frac{1}{2}\tilde{\theta}^T\boldsymbol{\Gamma}_2\tilde{\theta} + \frac{1}{2}\gamma^2. \tag{15}$$

Due to the fact that the system (12) has a cascaded structure, V can be considered as two parts, V_1 and V_2.

First,

$$V_1 = \frac{1}{2}\mathbf{r}^T\boldsymbol{\Gamma}_1\mathbf{r} + \mathbf{L}^T\boldsymbol{\Lambda}\mathbf{L} + \frac{1}{2}\tilde{\theta}^T\boldsymbol{\Gamma}_2\tilde{\theta} \tag{16}$$

where $\mathbf{L} = [\sqrt{\ln\cos h(\alpha_1\Phi_1)}\ \sqrt{\ln\cos h(\alpha_2\Phi_2)}]^T$. $\boldsymbol{\Lambda} = \mathrm{diag}(\alpha_1^{-1}\ \alpha_2^{-1})$ is a positive-definite and diagonal gain matrix. Next, define $\chi = [\mathbf{r}^T, \boldsymbol{\Phi}^T, \tilde{\theta}^T]^T$, denote the initial value of χ by $\chi_0 = [\mathbf{r}^T(t_0), \boldsymbol{\Phi}^T(t_0), \tilde{\theta}^T(t_0)]^T$, and let $||\mathbf{r}(t_0)|| = \delta_0$. Therefore, the differential of (16) is

$$\dot{V}_1 = \mathbf{r}^T\boldsymbol{\Gamma}_1\dot{\mathbf{r}} + (-\mathbf{K}_3\boldsymbol{\Psi} - \mathbf{K}_2\mathbf{r})^T\boldsymbol{\Pi} + \tilde{\theta}^T\boldsymbol{\Gamma}_2\dot{\tilde{\theta}}. \tag{17}$$

The details of derivation are shown in Appendix. According to Assumption 1 and the fact that ω_f is bounded due to physical limits, $||\mathbf{F}||$ and $||\dot{\mathbf{F}}||$ in (31) are bounded. Then, (31) in Appendix can be rewritten as

$$\begin{aligned}\dot{V}_1 \leq\ & -\mathbf{K}_3\boldsymbol{\Psi}^T\boldsymbol{\Pi} \\ & - \left[\lambda_{\min}(\boldsymbol{\Gamma}_1\mathbf{K}_4) - \lambda_{\max}(\mathbf{K}_5)||\tilde{\theta}||\right]\left\|\frac{\partial U}{\partial\hat{\theta}}\right\||\mathbf{r}||^2 \\ & - \Bigg[\lambda_{\min}(\boldsymbol{\Gamma}_1\mathbf{K}_1 + \boldsymbol{\Gamma}_1\mathbf{K}_2) \\ & - \frac{\lambda_{\max}(\Gamma_1\mathbf{s})\dot{f}_{\max} + \lambda_{\max}(\boldsymbol{\Gamma}_1\mathbf{k})f_{\max}}{||\mathbf{r}||}\Bigg]||\mathbf{r}||^2\end{aligned} \tag{18}$$

where $f_{\max}$ and $\dot{f}_{\max}$ denote the upper bounds of $\|\mathbf{F}(\gamma, \mathbf{u}_l)\|$ and $||\dot{\mathbf{F}}(\gamma, \mathbf{u}_l)||$, respectively. $-\mathbf{K}_3\boldsymbol{\Psi}^T\boldsymbol{\Pi} \leq 0$ because it is an odd function of $\boldsymbol{\Phi}$. The gains $\lambda_{\min}(\boldsymbol{\Gamma}_1\mathbf{K}_1 + \boldsymbol{\Gamma}_1\mathbf{K}_2)$ are chosen such that

$$\lambda_{\min}(\boldsymbol{\Gamma}_1\mathbf{K}_1 + \boldsymbol{\Gamma}_1\mathbf{K}_2) = \frac{\lambda_{\max}(\boldsymbol{\Gamma}_1\mathbf{s})\dot{f}_{\max} + \lambda_{\max}(\boldsymbol{\Gamma}_1\mathbf{k})f_{\max}}{\delta_\sigma}. \tag{19}$$

Let χ_σ represent the states when (19) is satisfied, where $||\mathbf{r}|| = \delta_\sigma < \delta_0$. It is noted that when $\delta_\sigma \leq ||\mathbf{r}|| \leq \delta_0$, the third term at the right-hand side of (18) is nonpositive. According to (16)

$$V_1(t) \geq \frac{1}{2}\tilde{\theta}^T\boldsymbol{\Gamma}_2\tilde{\theta} \geq \frac{1}{2}\lambda_{\min}(\boldsymbol{\Gamma}_2)||\tilde{\theta}||^2. \tag{20}$$

Thus, if the gains $\lambda_{\min}(\boldsymbol{\Gamma}_1\mathbf{K}_4)$ and $\lambda_{\max}(\mathbf{K}_5)$ are selected as

$$\frac{\lambda_{\min}(\boldsymbol{\Gamma}_1\mathbf{K}_4)}{\lambda_{\max}(\mathbf{K}_5)} > \sqrt{\frac{2V_1(t_0)}{\lambda_{\min}(\boldsymbol{\Gamma}_2)}} \tag{21}$$

then $\dot{V}_1 < 0$, and therefore, $V_1(t) < V_1(t_0)$ according to (18). So,

$$\frac{\lambda_{\min}(\boldsymbol{\Gamma}_1\mathbf{K}_4)}{\lambda_{\max}(\mathbf{K}_5)} > \sqrt{\frac{2V_1(t)}{\lambda_{\min}(\boldsymbol{\Gamma}_2)}} \geq ||\tilde{\theta}(t)|| \tag{22}$$

is satisfied when $||\chi_\sigma|| \leq ||\chi|| \leq ||\chi_0||$. This means that the second term on the right-hand side of (18) is nonpositive when $||\chi_\sigma|| \leq ||\chi|| \leq ||\chi_0||$, simply because

$$\lambda_{\min}(\boldsymbol{\Gamma}_1\mathbf{K}_4) - \lambda_{\max}(\mathbf{K}_5)||\tilde{\theta}|| \geq 0. \tag{23}$$

The analysis of the second term is similar to what is described in [23]. Moreover, there exists $0 < \delta_\tau < \delta_\sigma$ such that when $\|\mathbf{r}\| = \delta_\tau$, the third term is positive, and the magnitude of the third positive term is equal to the sum of magnitudes of first and second negative terms, i.e., $\dot{V}_1 = 0$. Let χ_τ represent the states resulting in $\dot{V}_1(\chi) = 0$. Then, $||\chi_\tau|| < ||\chi_\sigma|| < ||\chi_0||$. In other words, $\dot{V}_1$ is negative when $||\chi_\tau|| < ||\chi|| \leq ||\chi_0||$.

Based on the Lyapunov analysis of uniformly ultimately boundedness [24], solutions starting in the set $\{V_1(\chi) \leq V_1(\chi_0)\}$ will stay therein for all future time since $\dot{V}_1(\chi) < 0$ on the boundary $V_1(\chi_0)$. Moreover, for an arbitrary constant ε such that $V_1(\chi_\tau) < \varepsilon < V_1(\chi_0)$, $\dot{V}_1(\chi)$ will be negative in the set $\{\varepsilon \leq V_1(\chi) \leq V_1(\chi_0)\}$. In other words, $V_1(\chi)$ will decrease monotonically until the solution enters the set $\{V_1(\chi) \leq \varepsilon\}$. From then on, solutions cannot leave the set $\{V_1(\chi) \leq \varepsilon\}$ because $\dot{V}_1(\chi) < 0$ on the boundary ε. Thus, kit is concluded that the solution is uniformly ultimately bounded with the ultimate bound $||\chi|| \leq ||\chi_\varepsilon||$, where χ_ε represent the states resulting in $V_1(\chi) = \varepsilon$. What's more, according to (19), δ_σ can be shrunk small enough by increasing gains $\lambda_{\min}(\boldsymbol{\Gamma}_1\mathbf{K}_1 + \boldsymbol{\Gamma}_1\mathbf{K}_2)$, which means that δ_τ, $||\chi_\tau||$, and bound $||\chi_\varepsilon||$ can be small enough along with the decreasing of δ_σ. Therefore, the image-based error $\mathbf{r} = \mathbf{s}\Delta\dot{\mathbf{y}} + \mathbf{k}\Delta\mathbf{y} + \boldsymbol{\Phi}$ and $\boldsymbol{\Phi}$ can converge to a small enough set. At the equilibrium boundary where $\dot{V}_1(\chi) = 0$, there exists $\Delta\dot{\mathbf{y}} = \mathbf{0}$. So, $\Delta\mathbf{y}$ can be within the small enough set at the same time. Thus, the convergence of the image errors is ensured.

Second, to complete the proof, the stability analysis of internal dynamic of the leader–follower formation is considered next, hence,

$$V_2 = \frac{1}{2}\gamma^2. \tag{24}$$

The differential of (24) results in $\dot{V}_2 = \gamma\dot{\gamma}$. Because of the stability of $\Delta\mathbf{y}$, the position of the feature point P with respect to F_f, i.e., $({}^f x_P, {}^f z_P)$, can converge to the desired $({}^f x_{\mathrm{Pd}}, {}^f z_{\mathrm{Pd}})$. According to the position-based kinematic model given by (1), the angular velocity of the leader can be expressed as

$$\omega_f = \frac{\upsilon_l}{{}^f z_P}s_\gamma - \frac{1}{{}^f z_P}{}^f\dot{x}_P + \frac{1}{{}^f z_P}(-n_x s_\gamma + n_z c_\gamma)\omega_l. \tag{25}$$

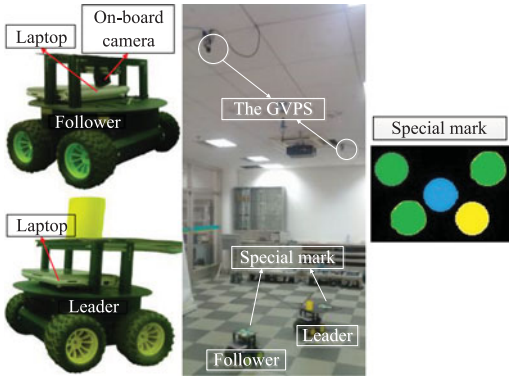

Fig. 4. Experimental system and the GVPS.

Then,

$$\dot{\gamma} = \omega_l - \omega_f = -\frac{v_l}{{}^f z_P} s_\gamma + \underbrace{\left(\frac{1}{{}^f z_P}({}^f z_P + n_x s_\gamma - n_z c_\gamma)\omega_l + \frac{1}{{}^f z_P}{}^f \dot{x}_P\right)}_{\eta_1}. \quad (26)$$

When $({}^f x_P, {}^f z_P)$ converges to the desired one, the nominal system $\dot{\gamma} = -v_l s_\gamma / {}^f z_P$ can be expressed as $\dot{\gamma} = -v_l s_\gamma / {}^f z_{\mathrm{Pd}}$, and it is exponentially stable when $v_l {}^f z_{\mathrm{Pd}} > 0$ is satisfied. Due to the boundedness of ω_l, s_γ, and c_γ and the stability of ${}^f z_P$ and ${}^f \dot{x}_P$, $|\eta_1| \le b_\eta$ is obtained. According to the stability theory of a perturbed system [24], when $\gamma(t_0) \neq \pm\pi$, the perturbed system (26) satisfies $|\gamma| \le b_\gamma$, i.e., γ is bounded. b_η and b_γ are positive constant related to the constants ${}^f z_{\mathrm{Pd}}$, $\bar{\omega}_l$, and $\mathbf{n}$. ■

Remark 5: When $v_l {}^f z_{\mathrm{Pd}} > 0$, $|\gamma| \le b_\gamma$ can be ensured. When $v_l {}^f z_{\mathrm{Pd}} < 0$ or $v_l = 0$, what the controller can achieve is only to guarantee convergence of $({}^f x_P, {}^f z_P)$.

IV. Experimental Results and Discussion

Two mobile robots were used for the physical experiments. Fig. 4 shows the setup of the experimental system. The size of the mobile robot is 40 cm × 40 cm × 30 cm. The rotation velocities of two wheels at the same side are controlled equally. An on-board perspective camera with 30-Hz sample frequency was connected to a laptop with a Pentium IV CPU. The low-level servo system with 50-ms period drives the wheels to the desired rotation speeds. The current velocity and acceleration of the robot, required by the observer, were calculated based on feedback from the encoders on the wheels. A global visual positioning system (GVPS) was developed to record the global trajectories of two robots in the world frame only. Both the controller and the observer do not need any global information. The GVPS is composed of two wide angle cameras fixed on the ceiling. The position, orientation, and ID information of the mobile robots were recognized by a special mark mounted on the top of the robots themselves. The accuracy of the GVPS for position and orientation are ±0.01 m and ±0.03 rad. The on-board camera's intrinsic and extrinsic parameters were both unknown. The position of feature point P on the leader was not measured. The communication between the two robots was ignored.

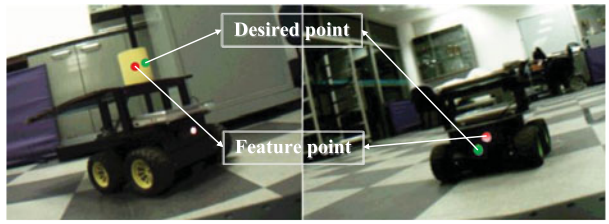

Fig. 5. Image from the on-board camera (a) first three experiments (b) last two experiments.

The first experiment was conducted to test the accuracy of the control algorithm using steady detection. The second one was aimed at testing stability and accuracy using relatively unsteady detection result. The third one was aimed at testing the robustness and limits of the control algorithm in extreme conditions.

In the first experiment, the leader moved in a line trajectory with velocity $v_l = 0.23$ m/s. A yellow cylinder was located at the leader's rotation center in order to represent the position of the leader's rotation center. The cylinder's height above the ground was not measured. Automatic threshold image segmentation was used to recognize the center of cylinder. The uncertainty of the detecting results was low, about ±2 pixels. The processing period is 64 ms. The desired position of P with respect to F_f $({}^f x_{\mathrm{Pd}}, {}^f z_{\mathrm{Pd}})$ was (0 m, 1 m), and the corresponding desired image point (y_{1d}, y_{2d}) was (303 pixels, 145 pixels). The true values of q are unknown, and the differences between the initial values of $\hat{q}$ and the roughly measured q are more than 100% of roughly measured q. The initial estimated parameters are $\hat{q}(t_0) = [\ 1,\ 1,\ -0.015,\ 0.004,\ -1000,\ -1,\ 0,\ 0,\ 0.001,\ 1000,\ -1,\ 10,\ -1000,\ -0.1,\ -0.1,\ 100\ ]^T$. The control gains are $\mathbf{K}_1 = \mathrm{diag}(2,5)$, $\mathbf{K}_2 = \mathrm{diag}(12,12)$,$\mathbf{K}_3 = \mathrm{diag}(0.01, 0.2)$, $\mathbf{K}_4 = 10^{-4}\mathbf{I}_{2\times 2}$, $\mathbf{K}_5 = 10^{-4}\mathbf{I}_{16\times 16}$,$\Gamma_1 = \mathrm{diag}(0.001, 0.005)$, $\Gamma_2 = \mathrm{diag}(10^{-5},\ 10^{-5},\ 10^{-10},\ 10^{-10},\ 10^{-3},\ 10^{-7},\ 10^{-10},\ 10^{-11},\ 10^{-12},\ 10^{-3},\ 10^{-7},\ 10^{-5},\ 10^{-3},\ 10^{-7},\ 10^{-7},\ 10^{-3})$, $\mathbf{s} = \mathrm{diag}(0.005, 0.09)$ and $\mathbf{k} = \mathrm{diag}(0.001, 0.09)$, $\alpha_1 = 3$ and $\alpha_2 = 3$, where $\mathbf{K}_1 = \mathrm{diag}(2,5)$. For example, this denotes that the first and the second diagonal element of the gain matrix $\mathbf{K}_1$ are 2 and 5, respectively.

The gains in the controller and observer were tuned experimentally. There are some empirical guidelines. First, the control gains in the controller, *i.e.*, $\mathbf{K}_1$, $\mathbf{K}_2$, $\mathbf{K}_3$, $\mathbf{k}$, and $\mathbf{s}$, were tuned to get a stable system. Next, the estimated parameters of the true values were set and the observer was turned OFF. Then, $\mathbf{K}_1$, $\mathbf{K}_2$, $\mathbf{K}_3$, $\mathbf{k}$, and $\mathbf{s}$ were selected by starting from small values and were increased slightly to get the satisfied tracking performance. Finally, the observer was turned ON and the same control gains were then used. Meanwhile, the estimated parameters were set to the initial estimated values and the observer gains were tuned by starting from small values. In general, the control responses are more sensitive to the gains $\mathbf{K}_1$, $\mathbf{K}_2$, $\mathbf{K}_3$, and $\mathbf{s}$.

Fig. 5(a) shows an example image from the on-board camera for the three experiments. The experimental results are shown in Fig. 6. In particular, Fig. 6(a) shows the trajectory of the center of the mark on the image plane. Fig. 6(b) shows the two robots' global trajectories, which were recorded by the GVPS. The initial point marked by the rhombus in Fig. 6(a) corresponds to the initial positions in Fig. 6(b). The center of

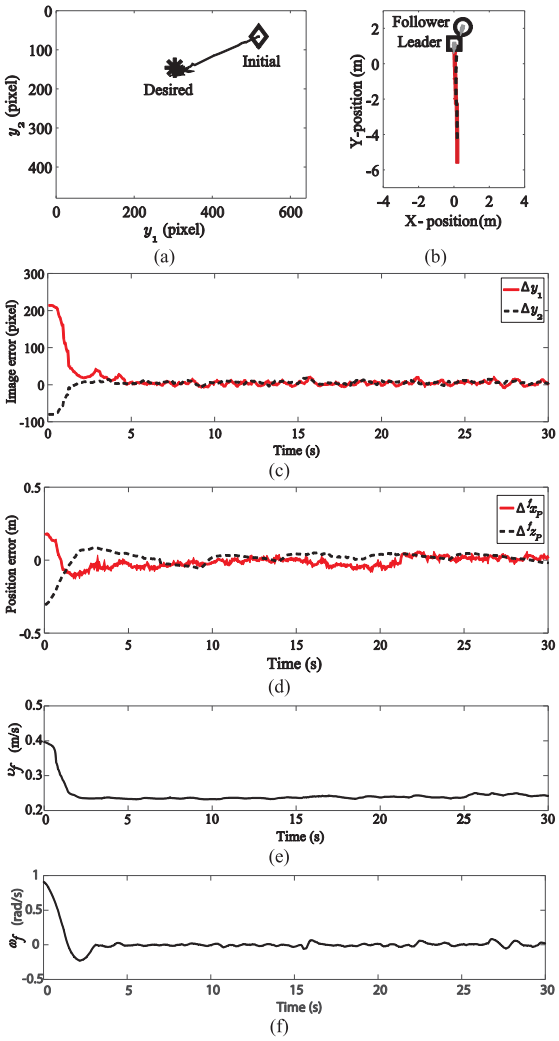

Fig. 6. Results of the first experiment: (a) image trajectory, (b) global trajectory in the world frame, (c) image error, (d) formation error, (e) control action of linear velocity to the follower, and (f) control action of angular velocity to the follower.

the mark converges to the desired point, marked by a star in Fig. 6(a), when the follower locks onto the leader at the desired position defined in the follower frame after about 5 s. Fig. 6(c) and (d) confirms the stable convergence of the image error as well as the formation error. Fig. 6(e) and (f) shows the control actions to the follower. The mean of the image errors and the formation error, which are defined as $\Delta^f z_P = {}^f z_P - {}^f z_{\mathrm{Pd}}$ and $\Delta^f x_P = {}^f x_P - {}^f x_{\mathrm{Pd}}$, and the variance are shown in Table I. These measures were calculated when the errors stabilized, *i.e.*, after about 15 s. The results show the performance of the controller with fast convergence of the errors. It is noted that the estimated parameters may not converge to the real values, but to some fraction of the real values. However, their variances and unmatched with the truths do not obstruct the convergence of image errors according to the proof of Theorem 1. The estimated parameters $\hat{q}$ are updated according to the observer control loop. The estimated parameters in the last loop are also utilized for the updating. Then, the updated $\hat{q}$ is sent to the controller to calculate the control signal for the follower (14) at the beginning to each.

TABLE I
STATISTICS OF THE EXPERIMENTAL RESULTS

	First Experiment	Second Experiment
Detection uncertainty	± 2 pixel	± 7 pixel
Image error	$\Delta\bar{y}_1 \approx 1.73$ pixel	$\Delta\bar{y}_1 \approx -3.74$ pixel
	$\Delta\bar{y}_2 \approx 3.11$ pixel	$\Delta\bar{y}_2 \approx -5.91$ pixel
	$S_{\Delta\bar{y}_1} \approx 0.22$ pixel	$S_{\Delta\bar{y}_1} \approx 0.50$ pixel
	$S_{\Delta\bar{y}_2} \approx 0.18$ pixel	$S_{\Delta\bar{y}_2} \approx 0.31$ pixel
Formation error	$\Delta^f\bar{x}_P \approx 0.01$ m	$\Delta^f\bar{x}_P \approx 0.01$ m
	$\Delta^f\bar{z}_P \approx 0.03$ m	$\Delta^f\bar{z}_P \approx 0.07$ m

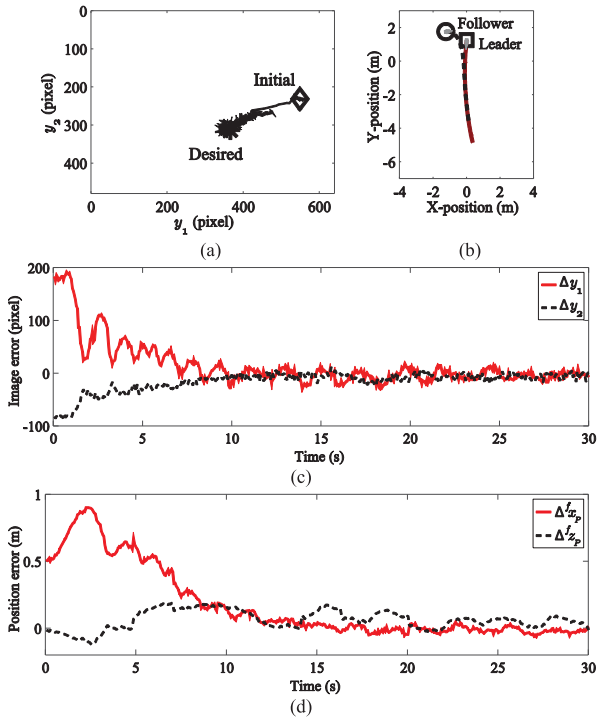

Fig. 7. Results of the second experiment: (a) image trajectory, (b) global trajectory in the world frame, (c) image error, and (d) formation error.

In the second experiment, a window-based BRISK keypoint detector [25] was used to detect a feature point on the leader. The uncertainty of the detecting results is around ± 7 pixels. The processing period is 50 ms. The leader moves in a line trajectory with $v_l = 0.23$ m/s. The desired position of P with respect to F_f $({}^f x_{\mathrm{Pd}}, {}^f z_{\mathrm{Pd}})$ is (0 m, 1 m), and the corresponding desired image point (y_{1d}, y_{2d}) is (365 pixel, 313 pixel). The initial estimated parameters are $\hat{q}(t_0) = [-5, -5, 0.015, 0.004, 1000, -1, 0, 0, 0.001, 1000, -1, -10, 1000, -0.1, -0.1, 100]^T$. The control gains are the same as the ones in the first experiment. Fig. 5(b) shows an example image from the on-board camera for this experiment. Fig. 7(a) shows the straight image trajectory. Fig. 7(b) shows the smooth global trajectory and the formation recorded by the GVPS. Fig. 7(c) and (d) confirms the stable convergence of the image error as well as the formation error. The results of the image errors and the formation error are shown in Table I. These values were calculated when the errors stabilized, *i.e.*, after about 10 s. The results show the stability and performance of the control algorithm where uncertainty was present.

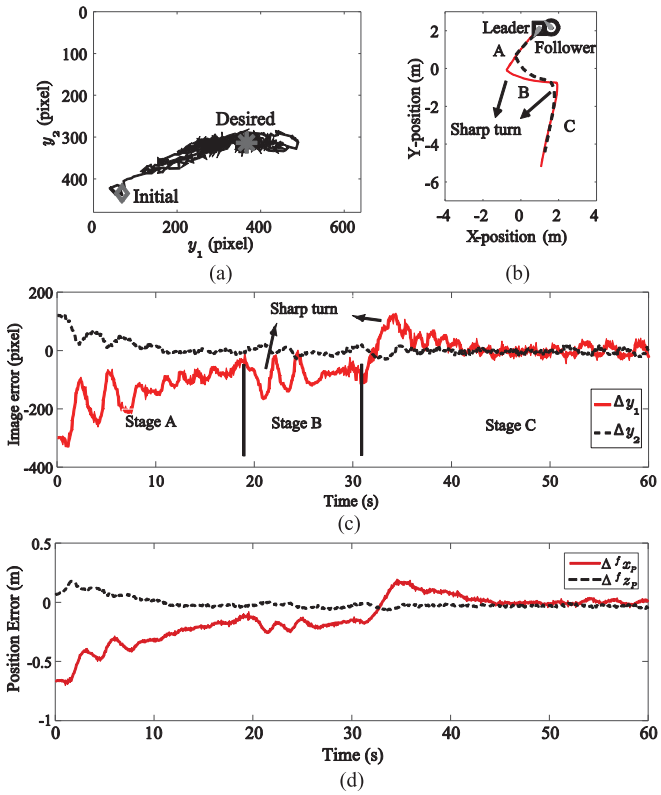

Fig. 8. Results of the third experiment: (a) image trajectory, (b) global trajectory in the world frame, (c) image error, and (d) formation error.

In the third experiment, the window-based BRISK keypoint detector was utilized. The leader's trajectory, which consists of three stages, is shown in Fig. 8(b). During stage A, $v_l = 0.15$ m/s. At the beginning of stage B, a sharp turn occurred with $v_l = 0$ and $\omega_l = -1.05$ rad/s. Then, the leader moves relatively fast with $v_l = 0.31$ m/s. In stage C, a similar sharp turn reappeared, and then, $v_l = 0.15$ m/s. The desired image point (y_{1d}, y_{2d}) is (303 pixel, 145 pixel). The initial estimated parameters are same as the second experiment. The gains are the $\mathbf{K}_1 = \text{diag}(1,3)$, $\mathbf{K}_2 = \text{diag}(8,8)$, $\mathbf{K}_3 = \text{diag}(0.01, 0.2)$, $\mathbf{K}_4 = 10^{-4}\mathbf{I}_{2\times 2}$, $\mathbf{K}_5 = 10^{-4}\mathbf{I}_{16\times 16}$, $\Gamma_1 = \text{diag}(0.001, 0.005)$, $\Gamma_2 = \text{diag}(10^{-5}, 10^{-5}, 10^{-10}, 10^{-10}, 10^{-3}, 10^{-7}, 10^{-10}, 10^{-11}, 10^{-12}, 10^{-3}, 10^{-7}, 10^{-5}, 10^{-3}, 10^{-7}, 10^{-7}, 10^{-3})$, $\mathbf{s} = \text{diag}(0.004, 0.04)$, $\mathbf{k} = \text{diag}(0.001, 0.09)$, $\alpha_1 = 3$, and $\alpha_2 = 3$.

There were three challenges in the third experiment: 1) the large initial image errors; 2) the sudden turn and fast response in the leader; and 3) instability in the detection. However, under the proposed control algorithm, these challenges did not lead to instability in the system. The image trajectory, shown in Fig. 8(a), shows that P can be locked in the middle of the field of view for all time. The image error curve in stage C, shown in Fig. 8(c), shows that stable convergence of the image error is still achieved despite the challenges. Finally, the results in Fig. 8(d) shows that the formation error convergences.

It is pointed out that the proposed control scheme is limited by visibility issues. Formation control will fail if the feature point cannot be detected successfully due to fast lateral movement of the leader. In particular, the lateral movement of the leader at the beginning of stage B should not exceed 0.35 m/s. Higher velocity causes blurring in the image, leading to failure in keypoint's detection capabilities, or the direct loss of P. In summary, the feature point should be selected such that it can be observed by the camera from any point of view.

V. Conclusion

This paper proposed an adaptive vision-based leader–follower formation controller for mobile robots. An on-board pin-hole camera can be mounted at any position and orientation on the follower, and the intrinsic and extrinsic parameters are uncalibrated. A feature point is selected at an arbitrary position on the leader, and its position and height are unknown. An adaptive observer is developed to estimate the unknown camera parameters and the coefficients of the plane in which the feature point moves with respect to the camera frame. An adaptive image-based controller is developed to lock onto the feature point on the leader at a desired position on the image plane, independent of measurement, or estimation of the velocity of the leader. It was shown by the Lyapunov method that the vision-based leader–follower system is stable. Experimental results verified the robust performance of the proposed algorithm. Future work includes designing a dynamic controller for the system.

Appendix

1) The elements of $\mathbf{J}_{\text{ff}}$, $\mathbf{J}_{\text{lf}}$, $\mathbf{J}_{\text{fC}}$, and $\mathbf{J}_{\text{lC}}$ are shown in the following, where $\mathbf{n} = [n_x \ n_y \ n_z]^T$, R_{ij} denotes the element of the rotation matrix ${}^f\mathbf{R}_C$, in the ith row and in the jth column, ${}^f\mathbf{R}_C$ denotes the rotation matrix from F_C **to** F_f, and $\mathbf{m} = [m_x \ m_y \ m_z]^T$ denotes the coordinate of O_C in F_f. Additionally,

$$\mathbf{J}_{\text{ff}} = \begin{bmatrix} 0 & -{}^f z_P \\ 0 & 0 \\ -1 & {}^f x_P \end{bmatrix}; \qquad \mathbf{J}_{\text{lf}} = \begin{bmatrix} s_\gamma & -n_x s_\gamma + n_z c_\gamma \\ 0 & 0 \\ c_\gamma & -n_z s_\gamma - n_x c_\gamma \end{bmatrix}$$

$$\mathbf{J}_{\text{fC}} = \begin{bmatrix} -R_{31} & -R_{23}{}^C y_P + R_{22}{}^C z_P + R_{31} m_x - R_{11} m_z \\ -R_{32} & -R_{21}{}^C z_P + R_{23}{}^C x_P + R_{32} m_x - R_{12} m_z \\ -R_{33} & -R_{22}{}^C x_P + R_{21}{}^C y_P + R_{33} m_x - R_{13} m_z \end{bmatrix}$$

$$\mathbf{J}_{\text{lC}} = \begin{bmatrix} R_{11} s_\gamma + R_{31} c_\gamma & R_{11}(-n_x s_\gamma + n_z c_\gamma) - R_{31}(n_z s_\gamma + n_x c_\gamma) \\ R_{12} s_\gamma + R_{32} c_\gamma & R_{12}(-n_x s_\gamma + n_z c_\gamma) - R_{32}(n_z s_\gamma + n_x c_\gamma) \\ R_{13} s_\gamma + R_{33} c_\gamma & R_{13}(-n_x s_\gamma + n_z c_\gamma) - R_{33}(n_z s_\gamma + n_x c_\gamma) \end{bmatrix}.$$

2) A details of the repulsive potential field $U(\hat{\theta})$ and the continuous potential force $\partial U(\hat{\theta})/\partial\hat{\theta}$ are

$$U(\hat{\theta}) = \begin{cases} \frac{1}{\exp(\kappa_2 p^2) - 1 + \kappa_1}, & |p| < \varepsilon_1 \\ 0, & |p| \geq \varepsilon_1 \end{cases}$$

$$\frac{\partial U(\hat{\theta})}{\partial \hat{\theta}} = \begin{cases} -\frac{2\kappa_2 p \exp(\kappa_2 p^2)}{(\exp(\kappa_2 p^2) - 1 + \kappa_1)^2} \frac{\partial p}{\partial \hat{\theta}}, & |p| < \varepsilon_1 - \varepsilon_2 \\ -\frac{\zeta}{\varepsilon_2}(\varepsilon_1 - |p|) p \frac{\partial p}{\partial \hat{\theta}}, & \varepsilon_1 - \varepsilon_2 \leq |p| \leq \varepsilon_1 \\ 0, & |p| > \varepsilon_1 \end{cases}$$

where ε_1, ε_2, κ_1, and κ_2 are all positive constants and $\zeta = 2\kappa_2 \exp(\kappa_2(\varepsilon_1 - \varepsilon_2)^2)/(\exp(\kappa_2(\varepsilon_1 - \varepsilon_2)^2) - 1 + \kappa_1)^2$.

3) The formula derivation in Section III-D is presented as follows, where (12) is rewritten in order to factor out $\tilde{q} = \hat{q} - q$, hence,

$$\begin{aligned}\dot{\mathbf{r}} = \; & \mathbf{s}\hat{\mathbf{H}}\dot{\mathbf{u}}_f + (\mathbf{s}\dot{\hat{\mathbf{H}}} + \mathbf{k}\hat{\mathbf{H}})\mathbf{u}_f - (\mathbf{s}\hat{\mathbf{H}} - \mathbf{s}\mathbf{H})\dot{\mathbf{u}}_f \\ & - \left((\mathbf{s}\dot{\hat{\mathbf{H}}} + \mathbf{k}\hat{\mathbf{H}}) - (\mathbf{s}\dot{\mathbf{H}} + \mathbf{k}\mathbf{H})\right)\mathbf{u}_f \\ & + \mathbf{s}\dot{\mathbf{F}} + \mathbf{k}\mathbf{F} - \mathbf{K}_3\boldsymbol{\Psi} - \mathbf{K}_2\mathbf{r}. \end{aligned} \tag{27}$$

Substituting (27) into (17) results in

$$\begin{aligned}\dot{V}_1 = \; & \mathbf{r}^T\boldsymbol{\Gamma}_1\Big\{\mathbf{s}\hat{\mathbf{H}}\dot{\mathbf{u}}_f + (\mathbf{s}\dot{\hat{\mathbf{H}}} + \mathbf{k}\hat{\mathbf{H}})\mathbf{u}_f - (\mathbf{s}\hat{\mathbf{H}} - \mathbf{s}\mathbf{H})\dot{\mathbf{u}}_f \\ & - \left((\mathbf{s}\dot{\hat{\mathbf{H}}} + \mathbf{k}\hat{\mathbf{H}}) - (\mathbf{s}\dot{\mathbf{H}} + \mathbf{k}\mathbf{H})\right)\mathbf{u}_f \\ & + \mathbf{s}\dot{\mathbf{F}} + \mathbf{k}\mathbf{F} - \mathbf{K}_3\boldsymbol{\Psi} - \mathbf{K}_2\mathbf{r}\Big\} \\ & + (-\mathbf{K}_3\boldsymbol{\Psi} - \mathbf{K}_2\mathbf{r})^T\boldsymbol{\Pi} + \tilde{\theta}^T\boldsymbol{\Gamma}_2\dot{\hat{\theta}}. \end{aligned} \tag{28}$$

Then, replacing $[\,\dot{v}_f \;\; \dot{\omega}_f\,]^T$ in the first term of (28) with the controller given by (13), the result becomes

$$\begin{aligned}\dot{V}_1 = \; & \mathbf{r}^T\boldsymbol{\Gamma}_1\left\{-\mathbf{K}_1\mathbf{r} - \mathbf{K}_2\mathbf{r} + \mathbf{s}\dot{\mathbf{F}} + \mathbf{k}\mathbf{F} - \mathbf{K}_4\left\|\frac{\partial U}{\partial\hat{\theta}}\right\|\mathbf{r}\right. \\ & \left. - \; (\mathbf{s}\hat{\mathbf{H}} - \mathbf{s}\mathbf{H})\dot{\mathbf{u}}_f - \left((\mathbf{s}\dot{\hat{\mathbf{H}}} + \mathbf{k}\hat{\mathbf{H}}) - (\mathbf{s}\dot{\mathbf{H}} + \mathbf{k}\mathbf{H})\right)\mathbf{u}_f\right\} \\ & - \boldsymbol{\Psi}^T\mathbf{K}_3\boldsymbol{\Pi} + \tilde{\theta}^T\boldsymbol{\Gamma}_2\dot{\hat{\theta}}. \end{aligned} \tag{29}$$

Next, according to Property 1, (29) can be rewritten as

$$\begin{aligned}\dot{V}_1 = \; & \mathbf{r}^T\boldsymbol{\Gamma}_1\left(-\mathbf{K}_1\mathbf{r} - \mathbf{K}_2\mathbf{r} + \mathbf{s}\dot{\mathbf{F}} + \mathbf{k}\mathbf{F} - \mathbf{K}_4\left\|\frac{\partial U}{\partial\hat{\theta}}\right\|\mathbf{r}\right) \\ & - \mathbf{r}^T\boldsymbol{\Gamma}_1\left[\mathbf{s}\mathbf{M}(\mathbf{y},\dot{\mathbf{u}}_f) + \mathbf{s}\mathbf{N}(\mathbf{y},\dot{\mathbf{y}},\mathbf{u}_f) + \mathbf{k}\mathbf{M}(\mathbf{y},\mathbf{u}_f)\right]\tilde{\theta} \\ & - \boldsymbol{\Psi}^T\mathbf{K}_3\boldsymbol{\Pi} + \tilde{\theta}^T\boldsymbol{\Gamma}_2\dot{\hat{\theta}}. \end{aligned} \tag{30}$$

Finally, plugging in the observer (14), the result becomes

$$\begin{aligned}\dot{V}_1 = \; & -\mathbf{r}^T\boldsymbol{\Gamma}_1(\mathbf{K}_1 + \mathbf{K}_2)\mathbf{r} + \mathbf{r}^T\boldsymbol{\Gamma}_1(\mathbf{s}\dot{\mathbf{F}} + \mathbf{k}\mathbf{F}) \\ & - \boldsymbol{\Psi}^T\mathbf{K}_3\boldsymbol{\Pi} - \mathbf{r}^T\boldsymbol{\Gamma}_1\mathbf{K}_4\left\|\frac{\partial U}{\partial\hat{\theta}}\right\|\mathbf{r} \\ & + \mathbf{r}^T\mathbf{r}\tilde{\theta}^T\mathbf{K}_5\frac{\partial U}{\partial\hat{\theta}} \leq -\mathbf{K}_3\boldsymbol{\Psi}^T\boldsymbol{\Pi} - \mathbf{r}^T \\ & \times(\boldsymbol{\Gamma}_1\mathbf{K}_4 - ||\tilde{\theta}^T\mathbf{K}_5||\mathrm{I}_{2\times 2})\left\|\frac{\partial U}{\partial\hat{\theta}}\right\|\mathbf{r} \\ & - \left[\lambda_{\min}(\boldsymbol{\Gamma}_1\mathbf{K}_1 + \boldsymbol{\Gamma}_1\mathbf{K}_2)\right. \\ & \left. - \frac{\lambda_{\max}(\boldsymbol{\Gamma}_1\mathbf{k})||\mathbf{F}|| + \lambda_{\max}(\boldsymbol{\Gamma}_1\mathbf{s})||\dot{\mathbf{F}}||}{||\mathbf{r}||}\right]||\mathbf{r}||^2. \end{aligned} \tag{31}$$

REFERENCES

[1] L. Zhang, T. Ahamed, Y. Zhang, P. Gao, and T. Takigawa, "Vision-based leader vehicle trajectory tracking for multiple agricultural vehicles," *Sensors*, vol. 16, no. 4, p. 578, Apr. 2016, doi: 0.3390/s16040578.

[2] X. Chen and Y. Jia, "Adaptive leader-follower formation control of non-holonomic mobile robots using active vision," *IET Control Theory Appl.*, vol. 9, no. 8, pp. 1302–1311, May. 2015, doi: 10.1049/iet-cta.2014.0019.

[3] H. Poonawala, A. C. Satici, N. Gans, and M. W. Spong, "Formation control of wheeled robots with vision-based position measurement," in *Proc. Amer. Control Conf.*, Jun. 2012, pp. 3173–3178.

[4] A. Dani, N. Gans, and W. Dixon, "Position-based visual servo control of leader-follower formation using image-based relative pose and relative velocity estimation," in *Proc. Amer. Control Conf.*, Jun. 2009, pp. 5271–5276, doi: 10.1109/ACC.2009.5160698.

[5] R. Vidal, O. Shakernia, and S. Sastry, "Formation control of nonholonomic mobile robots with omnidirectional visual servoing and motion segmentation," in *Proc. IEEE Int. Conf. Robot. Autom.*, vol. 1, Sep. 2006, pp. 584–589, doi: 10.1109/ROBOT.2003.1241657.

[6] A. De Luca, G. Oriolo, and P. R. Giordano, "Feature depth observation for image-based visual servoing: Theory and experiments," *Int. J. Robot. Res.*, vol. 27, no. 10, pp. 1093–1116, Oct. 2008, doi: 10.1177/0278364908096706.

[7] M. Chueh, Y. L. W. Au Yeung, K. P. Lei, and S. S. Joshi, "Following controller for autonomous mobile robots using behavioral cues," *IEEE Trans. Ind. Electron.*, vol. 55, no. 8, pp. 3124–3132, Aug. 2008, doi: 10.1109/TIE.2008.922605.

[8] A. K. Das, R. Fierro, V. Kumar, J. P. Ostrowski, J. Spletzer, and C. J. Taylor, "A vision-based formation control framework," *IEEE Trans. Robot. Autom.*, vol. 18, no. 5, pp. 813–825, Oct. 2002, doi: 10.1109/TRA.2002.803463.

[9] B. Fidan, V. Gazi, S. Zhai, N. Cen, and E. Karatas, "Single-view distance-estimation-based formation control of robotic swarms," *IEEE Trans. Ind. Electron.*, vol. 60, no. 12, pp. 5781–5791, Dec. 2013, doi: 10.1109/TIE.2012.2236996.

[10] G. L. Mariottini *et al.*, "Vision-based localization for leader–follower formation control," *IEEE Trans. Robot.*, vol. 25, no. 6, pp. 1431–1438, Dec. 2009, doi: 10.1109/TRO.2009.2032975.

[11] F. Morbidi, G. L. Mariottini, and D. Prattichizzo, "Observer design via immersion and invariance for vision-based leader–follower formation control," *Automatica*, vol. 46, no. 1, pp. 148–154, Jan. 2010, doi: 10.1016/S0005-1098(09)00560-3.

[12] P. Huang, D. Wang, Z. Meng, F. Zhang, and Z. Liu, "Impact dynamic modelling and adaptive target capturing control for tethered space robots with uncertainties," *IEEE/ASME Trans. Mechatronics*, vol. 21, no. 5, pp. 2260–2271, Oct. 2016, doi: 10.1109/TMECH.2016.2569466.

[13] P. Huang, D. Wang, Z. Meng, F. Zhang, and J. Guo, "Adaptive postcapture backstepping control for tumbling tethered space robot–target combination," *J. Guid., Control Dyn.*, vol. 39, no. 1, pp. 150–156, Jan. 2016, doi: 10.2514/1.G001309.

[14] S. Hutchinson, G. D. Hager, and P. I. Corke, "A tutorial on visual servo control," *IEEE Trans. Robot. Autom.*, vol. 12, no. 5, pp. 651–670, Oct. 1996, doi: 10.1109/70.538972.

[15] F. Chaumette, "Potential problems of stability and convergence in image-based and position-based visual servoing," in *The Confluence of Vision and Control*. London, U.K.: Springer, Sep. 1998, pp. 66–78, doi: 10.1007/BFb0109663.

[16] H. Garcia de Marina, M. Cao, and B. Jayawardhana, "Controlling rigid formations of mobile agents under inconsistent measurements," *IEEE Trans Robot.*, vol. 31, no. 1, pp. 31–39, Feb. 2015, doi: 10.1109/TRO.2014.2373145.

[17] H. Wang, Y. H. Liu, W. Chen, and Z. Wang, "A new approach to dynamic eye-in-hand visual tracking using nonlinear observers," *IEEE/ASME Trans. Mechatronics*, vol. 16, no. 2, pp. 387–394, Apr. 2011, doi: 10.1109/TMECH.2009.2039941.

[18] D. Guo, W. Yim, and K. K. Leang, "Adaptive repetitive visual-servo control of a low-flying unmanned aerial vehicle with an uncalibrated high-flying camera," in *Proc. IEEE/RSJ Int. Conf. Intell. Robot. Syst.*, Oct. 2016, pp. 4258–4265.

[19] L. Consolini, F. Morbidi, D. Prattichizzo, and M. Tosques, "Leader-follower formation control of nonholonomic mobile robots with input constraints," *Automatica*, vol. 44, no. 5, pp. 1343–1349, May. 2008, doi: 10.1016/j.automatica.2007.09.019.

[20] R. Cui, S. S. Ge, B. V. E. How, and Y. S. Choo, "Leader follower formation control of under actuated AUVs with leader position measurement," in *Proc. IEEE Int. Conf. Robot. Autom.*, May 2009, pp. 979–984, doi: 10.1109/ROBOT.2009.5152566.
[21] J. Ghommam, H. Mehrjerdi, and M. Saad, "Robust formation control without velocity measurement of the leader robot," *Control Eng. Practice*, vol. 21, no. 8, pp. 1143–1156, Aug. 2013, doi: 10.1016/j.conengprac.2013.04.004.
[22] J. J. E. Slotine and W. Li, "On the adaptive control of robot manipulators," *Int. J. Robot. Res.*, vol. 6, no. 3, pp. 49–59, Sep. 1987, doi: 10.1177/027836498700600303.
[23] X. Liang, H. Wang, W. Chen, D. Guo, and T. Liu, "Adaptive image-based trajectory tracking control of wheeled mobile robots with an uncalibrated fixed camera," *IEEE Trans. Control Syst. Technol.*, vol. 23, no. 6, pp. 2266–2282, Nov. 2015, doi: 10.1109/TCST.2015.2411627.
[24] H. K. Khalil, *Nonlinear systems*, vol. 4 & 9, 3rd ed. Upper Saddle River, NJ, USA: Prentice-Hall, 2011.
[25] S. Leutenegger, M. Chli, and R. Y. Siegwart, "BRISK: Binary robust invariant scalable keypoints," in *Proc. IEEE Int. Conf. Comput. Vis.*, Nov. 2011, pp. 2548–2555, doi: 10.1109/ICCV.2011.6126542.

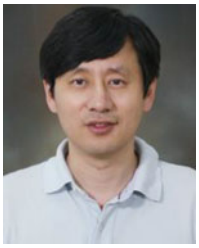

Hesheng Wang (SM'15) received the B.Eng. degree in electrical engineering from Harbin Institute of Technology, Harbin, China, in 2002, and the M.Phil. and Ph.D. degrees in automation and computer-aided engineering from The Chinese University of Hong Kong, Hong Kong, in 2004 and 2007, respectively.

From 2007 to 2009, he was a Postdoctoral Fellow and Research Assistant in the Department of Mechanical and Automation Engineering, The Chinese University of Hong Kong. He has been with Shanghai Jiao Tong University, Shanghai, China, since 2009, where he is currently a Professor in the Department of Automation. He was a Visiting Professor at the University of Zürich, Zürich, Switzerland. His research interests include visual servoing, service robotics, robot control, and computer vision.

Prof. Wang is an Associate Editor of *Robotics and Biomimetics*, *Assembly Automation*, *International Journal of Humanoid Robotics*, and IEEE TRANSACTIONS ON ROBOTICS. He served as an Associate Editor on the Conference Editorial Board of the IEEE Robotics and Automation Society from 2011 to 2015. He is the Program Chair of the 2019 IEEE/ASME International Conference on Advanced Intelligent Mechatronics.

Dejun Guo (S'16) received the B.Eng. degree in electrical engineering from Northwestern Polytechnical University, Xi'an, China, in 2012, and the M.S. degree in control engineering from the Department of Automation, Shanghai Jiao Tong University, Shanghai, China, in 2015. He is currently working toward the Ph.D. degree in mechanical engineering at the University of Utah, Salt Lake City, UT, USA.

He is also with the DARC (Design, Automation, Robotics & Control) Lab, University of Utah Robotics Center. His research interests include control systems, nanopositioning, and visual servoing.

Xinwu Liang received the B.S. and Ph.D. degrees in control engineering from Huazhong University of Science and Technology, Wuhan, China, in 2006 and 2011, respectively.

He was a Postdoctoral Fellow in the Department of Automation, Shanghai Jiao Tong University, Shanghai, China, from 2011 to 2014, and in the Department of Mechanical and Automation Engineering, The Chinese University of Hong Kong, Hong Kong, from 2014 to 2015. He is currently an Associate Professor with the School of Aeronautics and Astronautics, Shanghai Jiao Tong University. His current research interests include robot control, visual servoing, adaptive control, and computer vision.

Weidong Chen received the B.S. and M.S. degrees in control engineering, in 1990 and 1993, respectively, and the Ph.D. degree in mechatronics in 1996, all from Harbin Institute of Technology, Harbin, China.

Since 1996, he has been with Shanghai Jiao Tong University, Shanghai, China, where he is currently a Professor and the Head of the Department of Automation, and the Director of the Institute of Robotics and Intelligent Processing. He is also the Founder of the Autonomous Robot Laboratory, Shanghai Jiao Tong University. He was a Visiting Professor with the Artificial Intelligence Laboratory, University of Zürich, Zürich, Switzerland, in 2012. He has been a Visiting Professor in the Brain Science Life Support Research Center, University of Electro-Communications, Chofu, Japan, since 2016. His current research interests include autonomous robotics, assistive robotics, and medical robotics.

Guoqiang Hu received the B.Eng. degree in automation from the University of Science and Technology of China, Hefei, China, in 2002, the M.Phil. degree in automation and computer-aided engineering from The Chinese University of Hong Kong, Hong Kong, in 2004, and the Ph.D. degree in mechanical engineering from the University of Florida, Gainesville, FL, USA, in 2007.

He is currently with the School of Electrical and Electronic Engineering, Nanyang Technological University, Singapore. Prior to his current position, he was a Postdoctoral Research Associate with the University of Florida, in 2008, and an Assistant Professor at Kansas State University, Manhattan KS, USA, from 2008 to 2011. His current research interests include distributed control and optimization with applications to energy systems and multirobot coordination.

Kam K. Leang (M'02) received the B.S. and M.S. degrees in mechanical engineering from the University of Utah, Salt Lake City, UT, USA, in 1997 and 1999, respectively, and the Ph.D. degree from the University of Washington, Seattle, WA, USA, in December 2004.

He is an Associate Professor in the Mechanical Engineering Department, University of Utah, which he joined in July 2014. He is the Director of the DARC (Design, Automation, Robotics & Control) Lab, University of Utah Robotics Center. Between 2008 and 2014, he was with the University of Nevada, Reno, NV, USA. His research interests include modeling and precision control of electroactive (smart) material actuators (piezoelectrics and electroactive polymers), nanopositioning and scanning probe microscopy, and design, motion planning, and control of robotic systems.

Dr. Leang currently serves as an Associate Editor for the *IEEE Control Systems Magazine*, *Mechatronics*, *International Journal of Intelligent Robotics and Applications*, and *Frontiers in Mechanical Engineering*. He has served as an organizer and editor for various conferences, including the American Control Conference, IEEE International Conference on Robotics and Automation, and IEEE/ASME International Conference on Advanced Intelligent Mechatronics. He is a member of the American Society of Mechanical Engineers (ASME).